

Resubmission manuscript CEJ-S-22-00593

<https://doi.org/10.1016/j.cej.2022.136999>

Assessment of a catalytic plate reactor with in-situ sampling capabilities by means of CFD modeling and experiments.

*Varun Surendran¹, Mauro Bracconi², Jose A. Hernandez Lalinde¹, Matteo Maestri², and Jan Kopyscinski^{*1}.*

¹Department of Chemical Engineering, McGill University, 3610 University Street, Montreal, H3A 0C5, Quebec, Canada

²Laboratory of Catalysis and Catalytic Processes, Department of Energy, Politecnico di Milano via La Masa 34, 20156 Milano, Italy

* To whom all correspondence should be addressed:

jan.kopyscinski@mcgill.ca

Tel.: +1 514 398 4276

Abstract

A catalytic plate reactor with a small movable sampling capillary enables us to gather a significantly larger set of kinetic data for the parameter estimation than using a typical steady-state packed-bed reactor with end-of-pipe measurement. In this study, a reactive three-dimensional CFD model developed with catalyticFOAM is validated by experimental axial gas species concentration profiles and then used to investigate the flow dynamics and study the effect of the immersed capillary for various operating conditions for the CO₂ methanation reaction over Ni/Al₂O₃ catalyst. The results confirmed that the presence of the capillary (diameter 0.5 mm, continuous *vs.* open-ended) inside the rectangular channel (5 x 40 x 100 mm), the position of the orifice (diameter 0.2 mm), and the suction (2 to 8 ml/min) did not affect the quality of the kinetic data collected. For the current design of the reactor inlet, the flow fully develops within the first 10-25 mm of the reactor domain depending on the total flow rate (100 to 300 ml_N/min). Hence, up to 90% of the reactor's length can be used for in-situ measurements. This work demonstrates that our channel reactor is very suitable for collecting kinetic data, especially for fast and exothermic heterogeneous catalyzed reactions, with a high spatial resolution for gas composition and catalyst surface temperature.

Keywords: CFD modeling, catalytic plate reactor, catalyticFOAM, in-situ sampling.

1 Introduction

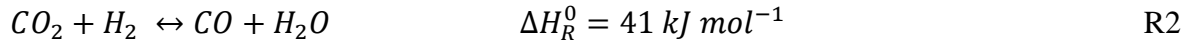
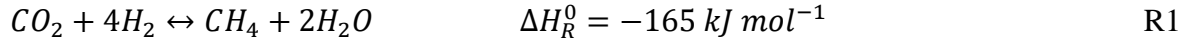
The design of chemical reactors for heterogeneous catalyzed reactions is challenging due to the coexistence of multiple complex intercoupled phenomena such as reactions, local flow, interfacial mass transfer, and heat transfer. A detailed understanding of reaction kinetics is one of the primary requirements for the design. The traditional approach to gather kinetic data involves small laboratory packed-bed reactors. They are usually operated as differential and/or integral reactors and yield only one data point per species per experiment by measuring the exit-gas composition under conditions where transport resistances are negligible. Differential reactors are usually limited to conversion values smaller than 20% relative to chemical equilibrium. Integral reactors can be operated with conversions of up to 90%. Heterogeneities like non-uniform catalyst mass distribution, concentration, and temperature gradients along the axial and radial directions make data collection and, thus, kinetic parameter estimation and model discrimination difficult. Gathering gas species data and temperatures along the reactor axis allows closing the knowledge gap as they combine differential and integral reactor information. In this respect, spatially-resolved measurements via movable capillaries and thermocouples along with spectroscopic in-situ measurements have been applied for monolith [1,2], coated metal foam [3,4], packed bed [5,6], fluidized bed [7,8], annular [9] and channel reactors [10,11]. Only for the latter, the catalyst mass distribution along the reactor axis can be determined via profilometry [12], which makes it very suitable for kinetic data collection [13]. However, the presence of a capillary (i.e., invasive technique) might influence the data acquisition. To assess the effect of the capillary on the system, multiscale computational fluid dynamics (CFD) simulations can be employed by providing a reliable approach to studying the influence. This approach has already been employed for the analysis of monolith-type systems equipped with in-situ sampling [14,15], revealing that the

sampling probe significantly reduces the cross-sectional area of the channel and influences the local fluid flow. Both, Hettel *et al.* [14,15] and Benzinger *et al.* [16] included detailed surface reactions in the CFD model and employed a single monolith channel from a reactor setup that used a monolith block with 600 channels per square inch with spatial measurement capabilities. The placement of the sampling probe in the corner of the monolith channel resulted in the smallest interference with bulk flow [14,15]. Benzinger *et al.* [16] investigated the operation of a similar monolith channel reactor, using Ansys Fluent and DUO CFD solvers for the reverse water gas shift reaction and observed a reasonable agreement between the CFD model prediction for all species except H₂. They also reported the influence of diffusion in the region upstream of the catalyst.

Our research group at McGill has developed an optically accessible catalytic plate reactor (CPR) for spatial profiling, which is a single channel equipped with an in-situ continuous capillary along the reactor axis [12]. This system is similar to the catalytic plate reactor developed by the Paul-Scherrer Institute (Switzerland), with an open-ended capillary supported on one side [10]. The open-ended capillary approach has been reported to face certain challenges due to bending at one end under its own weight [10]. Bosco *et al.* [9] developed a 2D/3D CFD non-reactive CFD model with heat transfer capabilities in FEMLAB to study hydrodynamics in that channel reactor, but they did not investigate the effect of the capillary and the influence of the suction on the flow field and kinetic data. Differently, our CPR is characterized by the presence of a continuous sampling capillary with a side sampling orifice that is supported at both ends of the reactor to prevent bending.

We have utilized the CPR setup to collect ~21,000 gas composition data to investigate the reaction mechanism and determine the corresponding kinetic parameters for the combined exothermic CO₂

methanation (R1) and endothermic reverse water gas shift (R2) reactions over Ni-alumina catalyst [13].



In the present work, the CPR's ability to collect high-quality kinetic data is quantitatively assessed. We have developed a reactive 3D CFD model with surface reactions expressed as Langmuir Hinshelwood kinetics using the CatalyticFOAM [17] and the OpenFOAM framework [18]. The CFD model includes vital geometric features like inlet manifold and inlet/outlet distributor channels. This detailed model aids in developing an accurate understanding of the influence of the sampling capillary in different regions of the CPR. The CFD model is validated based on experimental data (gas composition profiles) and used to study the effect of bulk flow rate and the capillary suction on the flow hydrodynamics on the kinetic data. This study establishes the CPR's optimum operation range and provides insights into the possible modifications for the next generation CPR.

2 Methodology

2.1 Experimental

2.1.1 Catalytic plate reactor (CPR)

The details of the setup are described in our previous work [12]. Briefly, the CPR's primary domain is a rectangular channel (z -direction = 100 mm, x -direction = 40 mm, y -direction = 5 mm) with a catalyst coated bottom plate (Fig. 1). For the current study, the catalyst is coated between 15 and 90 mm of the CPR domain's bottom plate. A movable sampling capillary (0.5 mm diameter with a 250 μm sampling orifice) is present along the length of the reactor (i.e., 2.0 mm above the catalyst

surface) and connected to a calibrated quadrupole mass spectrometer (Hiden Analytical, HPR-20, UK). This capillary is supported at both ends of the reactor to maintain a constant elevation from the coated surface along the entire reactor length. The sampling capillary is moved along the reactor axis by a linear positioning system (electric step motor controlled by LabVIEW™, accuracy < 0.1 mm). The capillary is long enough to assure that it is always supported on both ends, even when sampling along the complete channel.

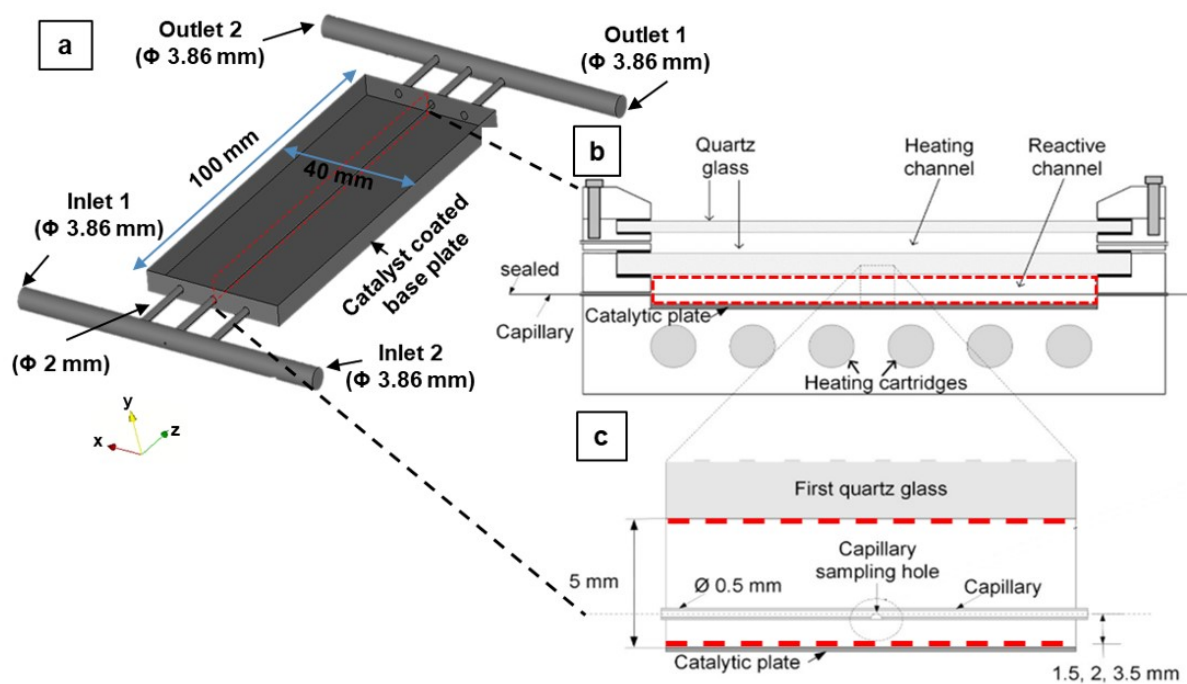


Fig. 1 Scheme of the catalytic plate reactor. (a) isometric domain view, (b) side view, and (c) detailed side-view. The dashed red line marks an axial slice of the CPR.

The top of the reactor is closed with fused quartz glass plates to enable catalyst surface temperature measurements via IR thermography (FLIR, SC2500, Burlington, ON, Canada). In addition, a second heating channel (5 mm height) is added above the reactive channel in which Ar at reaction temperature and a flow rate of 300 ml_N/min is fed counter-currently [12]. The second channel is closed on top by second quartz glass, maintaining optical accessibility for the IR thermography.

By doing so, temperature gradients along the height of the reactive channel are less than 5 °C for a catalyst surface temperature of 420 °C [13].

2.1.2 Catalyst and catalytic coating

An ordered mesoporous nickel-alumina catalyst with ~30 wt% NiO/Al₂O₃, a BET surface area of 90 m²/g, and a pore volume of 0.48 cm³/g is used. A detailed description of the catalyst preparation and coating can be found in [19] and [20], respectively. A homogenous coating with a thickness of 40-60 μm and length of 75 mm is obtained with a total catalyst loading of 100 to 110 mg.

2.1.3 Experimental procedure

The procedure for kinetic data acquisition is published in our previous work [13]. Briefly, the catalyst plate is loaded into the CPR and reduced with 20 vol% H₂ (99.999% MEGS Specialty Gases) in Ar (99.999% MEGS) at the reduction temperature (i.e., 560 °C) for 8 h. Then the reactor is brought to the operating temperature. Subsequently, the capillary orifice is moved to zero position (e.g., 15 mm before the coating begins). H₂ and CO₂ are then set to the desired flow rate, while Ar is used as an internal standard. The sampling capillary is held for 45–900 s at each position and moved in flow direction with a spatial resolution of 1 data point per millimeter above the coated area and per 2 mm above the non-coated area. Thus, up to 75 data points per gas species per experiment over the coated area are obtained. Validation experiments for this study are conducted at different total flow rates (100-150 mL_N/min) at 360 °C and 1.2-4 bar_{abs} for two different plates loaded with 103 and 112 mg of catalyst.

2.2 CFD model

2.2.1 CatalyticFOAM and heterogeneous catalysis

The flow phenomena in the CPR can be described by solving the conservation equations for mass, momentum, and species for a Newtonian fluid, as shown in Eqs. 1-3 [21].

$$\frac{d\rho}{dt} + \nabla(\rho v) = 0 \quad (1)$$

$$\frac{d}{dt}(\rho v) + \nabla \cdot (\rho v v) = -\nabla p + \nabla \cdot \left[\mu(\nabla v + \nabla v^T) - \frac{2}{3}\mu(\nabla v)I \right] + \rho g \quad (2)$$

$$\frac{d}{dt}(\rho \omega_k) + \nabla \cdot (\rho \omega_k v) = \nabla \cdot (\rho \omega_k V_k) \quad k = 1, \dots, \text{NCG} \quad (3)$$

where ρ is the density, v is the velocity vector, p is the operating pressure, g is the acceleration vector due to gravity, μ is the viscosity, ω_k is the mass fraction of gas-phase species k , I is the identity tensor and V_k is the diffusion velocity. The diffusion velocity is evaluated as described in detail in Maestri *et al.* [17] under the assumption of negligible Soret effect (see Eq. 4).

$$V_k = \frac{\Gamma_k}{\omega_k} \nabla \omega_k \quad (4)$$

The transport properties of the species are computed by using the standard kinetic theory expressions [22][23][24]. The evaluation of transport properties is performed through the mixture averaging rules. The heterogeneous reactions are accounted for by a boundary condition where the local mass flux of the species towards the wall is equal to the net formation rates due to the surface reactions (Eq. 5).

$$\rho \cdot \Gamma_{k,mix}(\nabla \omega_k) \Big|_{catalytic} = \frac{A_{cat}^{eff}}{A} \dot{\Omega}_k^{het} \quad k = 1, \dots, \text{NCG} \quad (5)$$

where ρ is the density, $\Gamma_{k,mix}$ is the individual species mixture averaged diffusion coefficient, A_{cat}^{eff} is the effective catalytic area and A is the geometric area.

The governing equations are implemented in the catalyticFOAM framework, a numerical solver for heterogeneous reactive flow based on the OpenFOAM. Additional details on the numerical implementation can be found in [17]. CatalyticFOAM has been successfully used for fast reactions, including hydrogen oxidation by Maestri *et al.*[17], where it has been demonstrated to provide accurate results in both chemical regimes and external mass transfer limited conditions [25] with respect to experimental data.

The solution development process is relatively simple with the CPR experiment inlet conditions of concentration, pressure, and temperature are defined at the inlet boundary at the beginning of the simulation. These inlet parameters are kept constant, and their evolution is monitored at the outlet continuously. The governing equations are solved to obtain the steady-state by using a SIMPLE scheme for pressure-velocity coupling as described in Micale *et al.* [26]. This simulation is stopped and considered converged once the flow evolution stabilizes, the outlet compositions are constant in time, and the atomic balances are closed.

The kinetics of the CO₂ methanation and reverse water gas shift (RWGS) reactions in the form of a Langmuir Hinshelwood rate expressions (Eqs. 6 and 7, [13]) were implemented in this CFD model.

$$r_{CO_2meth} = \frac{k_{CO_2meth} \cdot K_{COH} \cdot p_{CO_2}^{0.5} \cdot K_{H_2} \cdot p_{H_2} \cdot \left(1 - \left(\frac{p_{H_2O}^2 \cdot p_{CH_4}}{p_{H_2}^4 \cdot p_{CO_2} \cdot K_{eqM}} \right) \right)}{\left(1 + K_{COH} \cdot p_{CO_2}^{0.5} \cdot K_{H_2}^{0.5} \cdot p_{H_2}^{0.5} + \sqrt{K_{H_2} \cdot p_{H_2}} + K_{OH} \frac{p_{H_2O}}{\sqrt{p_{H_2}}} \right)^2} \quad (6)$$

$$r_{RWGS} = \frac{k_{RWGS} \cdot p_{CO_2} \cdot K_{H_2}^{0.5} \cdot p_{H_2}^{0.5} \cdot \left(1 - \left(K_{\beta} \cdot \frac{p_{CO} \cdot p_{H_2O}}{p_{H_2} \cdot p_{CO_2} \cdot K_{eqRWGS}}\right)\right)}{\left(1 + K_{COH} \cdot p_{CO_2}^{0.5} \cdot K_{H_2}^{0.5} \cdot p_{H_2}^{0.5} + \sqrt{K_{H_2} \cdot p_{H_2}} + K_{OH} \cdot \frac{p_{H_2O}}{\sqrt{p_{H_2}}}\right)^2} \quad (7)$$

where k_{CO_2meth} and k_{RWGS} are the reaction rate constants, K_i is the lumped parameter containing adsorption coefficients and elementary step rate constants, p_i is the partial pressure of CO₂, H₂, H₂O, CH₄, and K_{eq} the equilibrium constants. The kinetic model assumes that the rate-determining step is the second C–O bond cleavage, which is assisted by hydrogen (i.e., COH* + H* ↔ CH* + OH*) with the corresponding kinetic parameters summarized in Table 1 [13].

Table 1 Kinetic parameters for CO₂ methanation and RWGS [13].

Parameter	Units	Values
$k_{CO_2meth}(T_{ref})$	mol kg _{cat} ⁻¹ s ⁻¹ bar ^{-0.5}	0.80 ± 0.01
E_{A,CO_2meth}	kJ mol ⁻¹	79.7 ± 4.7
$k_{RWGS}(T_{ref})$	mol kg _{cat} ⁻¹ s ⁻¹ bar ⁻¹	0.19 ± 0.02
$E_{A,RWGS}$	kJ mol ⁻¹	194.7 ± 7.0
$K_{COH}(T_{ref})$	bar ^{-0.5}	2.77 ± 0.25
ΔH_{COH}	kJ mol ⁻¹	60.5 ± 7.9
$K_{H_2}(T_{ref})$	bar ⁻¹	0.24 ± 0.01
ΔH_{H_2}	kJ mol ⁻¹	-12.5 ± 2.0
$K_{OH}(T_{ref})$	bar ^{-0.5}	1.73 ± 0.16
ΔH_{OH}	kJ mol ⁻¹	64.4 ± 4.9
$K_{\beta}(T_{ref})$	-	4.52 ± 0.14
ΔH_{β}	kJ mol ⁻¹	-21.4 ± 2.1

As proven in our previous works, homogeneous gas-phase reactions can be neglected under the presented reaction condition [12,13].

2.2.2 Model domain

Fig. 1 shows the domain of the CPR incorporated into the CFD model. The primary domain is a combination of three zones, (1) upstream zone comprising of the lateral inlet pipe (3.86 mm

diameter) with two inlets that are connected to three distributor channels (2 mm diameter), (2) rectangular domain (100 mm long) with a catalyst coated bottom surface, and (3) downstream zone consisting of three collector channels leading to the lateral outlet pipe with two outlets. The upstream and downstream zones are included in the final CFD model domain as they impact the flow development in the rectangular reactor domain. The left, central and right distributor/collector channels are located at an elevation of 1.5, 2.0 and 3.5 mm from the bottom surface, respectively, enabling data collection of the gas species at a different height above the catalyst surface. This difference in the three distributors/collector channels' elevation prevents using a partial CPR domain via a plane of symmetry approach for this CFD study. The end-to-end sampling capillary passes through the middle of centrally located distributors/collector channels (at an elevation of 2.0 mm from the bottom surface). The flow inside the capillary after leaving the main CPR domain through the sampling port is not of interest. Hence, the region inside the capillary is not included in the CFD model domain. The presence of the capillary in the CPR domain is modeled through a no-slip wall boundary defined with the outer dimensions of the sampling capillary. The sampling port is defined as a circular face patch on the capillary wall, and for the current simulation it is located at 15 mm, 50 mm and 90 mm into the rectangular domain.

Four different design modifications including (i) upward and (ii) sideward orientation of capillary sampling orifice, (iii) open-ended capillary (Fig.S1), and (iv) dummy capillaries in the outer distributor channels are investigated. In the open-ended capillary case, the sampling capillary is not supported on both ends, it enters the reactor in the downstream section, and it is open at the other end as described in [11]. The geometries for the CFD model are generated using the open-source Salome CAD package [27].

2.2.3 Model specifications and boundary conditions

The flow in the CPR domain is assumed to be steady-state and in laminar conditions as the Reynolds numbers are between 0.1 to 2.0. The highest velocities are observed in the distributor channels with Reynolds numbers of max 1.8 for a characteristic length of 2 mm. Experiments showed that the maximum temperature differences along the reactor axis (inlet to outlet) and along with the channel height (catalyst surface to quartz plate) are 3 °C and 5 °C, respectively. [12]. Therefore, the flow is assumed to be isothermal for this study. CatalyticFOAM included the surface reaction via a catalytic wall of zero thickness, and hence the catalyst coating was not spatially resolved in this study. This assumption is proven to be valid due to the absence of mass transfer limitation in the catalyst coating [13].

The boundary conditions for the model are defined as:

- Inlet boundary conditions are defined on the two circular inlet faces present at either side of the inlet manifold with fixed values for velocity, zero gradient pressure boundaries, and fixed values for species composition.
- Outlet boundaries: zero gradients for velocity and species compositions and fixed value pressure.
- Sampling port patch: Capillary orifice suction is implemented with a fixed volumetric flow rate outlet boundary (`flowRateOutletVelocity`) and zero gradients for species and pressure.
- Inert walls: The mass flux of the individual species is set to zero, a no slip condition for velocity and zero gradient for pressure.
- Catalytic wall: The mass flux of the individual species is assumed equal to the formation rate due to the heterogeneous reaction occurring on the catalytic wall. [18]

The range of operating conditions used in the CFD model is listed in Table 2.

Table 2 CPR reactor CFD model operating conditions.

Parameter	Units	Plate #1	Plate #2
Catalyst loading	mg	103	112
Pressure	bar _{abs}	1.2	1.2 - 4
Temperature	°C	360 - 420	360
Inlet volumetric flowrates	mL _N /min	150	100 - 300
H ₂ /CO ₂ ratio		4; 5	5
Suction Orifice flow	mL/min	2	1 - 10
Inlet Mass fraction:			
H ₂		0.0549	0.0785
CO ₂		0.2405	0.4317
Ar		0.7046	0.4897

The mesh for the model is created using the snappyHexMesh utility of the OpenFOAM framework. The final selected mesh has a cell count of around 10 million cells. Mesh independent results are obtained by conducting the simulation at three different mesh resolution levels. The coarsest mesh contains approximately 4 million cells, and the most refined mesh contained 19 million cells (Fig.S2). It is observed that the CO₂ conversion at the outlets varied by less than 0.5% between the selected mesh and the most refined mesh (see supplementary material Fig.S3).

The numerical schemes are defined as follows. A second-order upwind (linear Upwind) scheme is employed for the convective terms, while second-order discretization is adopted for the Laplacian operator.

3 Results and discussions

3.1 Model validation

The CPR's spatial sampling capability enables a detailed validation of the 3D reactive CFD model. Fig. 2 shows the comparison CFD model predictions with the experimental data for a total flow rate of (a) 150 ml_N/min at 360 °C and 1.2 bar_{abs}, (b) 100 ml_N/min at 360 °C and 1.2 bar_{abs}, (c) 150 ml_N/min at 380 °C and 1.2 bar_{abs}, and (d) 100 ml_N/min at 360 °C and 4 bar_{abs}. The local species concentration values in the CFD model are extracted on a straight line along the length of the channel. The predicted gas species compositions for all cases show good agreement with the experimental data, and it confirms the successful implementation of the heterogeneous catalytic reactions for the CO₂ methanation process in the CFD model. The variation in H₂ predictions is attributed to the combined effects of kinetic model implementation, species diffusion and experimental measurement. As stated in our previous manuscript, the atomic C and O balances along the reactor axis were always closed with 5% error, whereas in some cases (especially at high pressure and temperatures), the H balances deviated up to 7% [13]. The kinetic parameters for the CO₂ methanation were determined using a simplified one-dimensional reactor model in which axial dispersion was neglected [13]. Especially at lower flow rates, the minor deviations can be ascribed to these simplifying assumptions, which causes slightly lower H₂ concentration before the catalyst coated area (Fig. 2b). This effect also results in the offset in H₂ predictions in case 4 bar_{abs} operating pressure case (Fig. 2d) as the increase in operating pressure results in a reduction in overall volumetric flow entering the reactor domain.

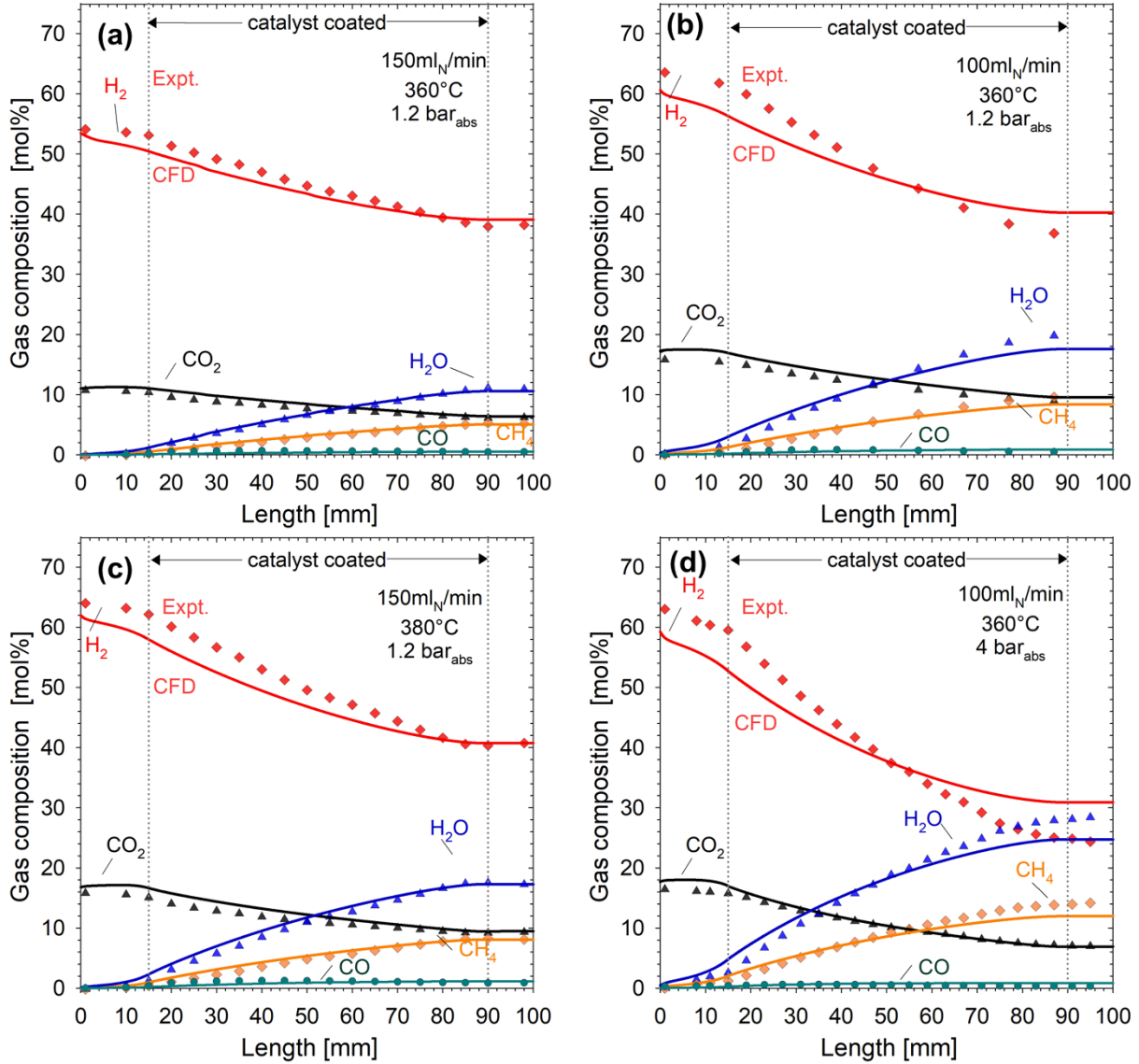


Fig. 2 Axial gas composition profile along the reactor axis for a total flow rate of (a) Plate 1 at 150 ml_N/min, 360 °C, 1.2 bar_{abs}, and H₂/CO₂ ratio of 5, (b) Plate 2 at 100 ml_N/min, 360 °C, 1.2 bar_{abs}, and H₂/CO₂ ratio of 4, (c) Plate 2 at 150 ml_N/min, 380 °C and 1.2 bar_{abs} and H₂/CO₂ ratio of 4, and (d) Plate 2 at 100 ml_N/min, 360 °C, 4 bar_{abs}, and H₂/CO₂ ratio of 4. Symbols and solid lines denote experimental data and the CFD model, respectively.

The model successfully captures the effect of the increase in temperature on the conversion in the CPR domain. Fig. 3 shows the comparison of the CFD model predictions for CO₂ molar fraction on a vertical slice along the center plane of the CPR domain for (a) 100 ml_N/min at 360 °C, (b) 150 ml_N/min at 380 °C, and (c) 150 ml_N/min at 420 °C. The CO₂ species profile along an axial line

for cases (a) and (b) is reported and validated in Fig. 3. CO₂ conversion of about 49% is obtained at the reactor exit for the 100 ml_N/min at 360 °C (Fig. 3a), and almost identical conversion is obtained for 150 ml_N/min at 380 °C even though it has 1.5 times higher flow rate entering the domain (Fig. 3b). Also, for 150 ml_N/min at 420 °C, the highest outlet CO₂ conversion of 62% is achieved in the reactor domain and the same is evident from the closely placed iso-contour lines in Fig. 3 that lead to a final outlet molar fraction of 0.07.

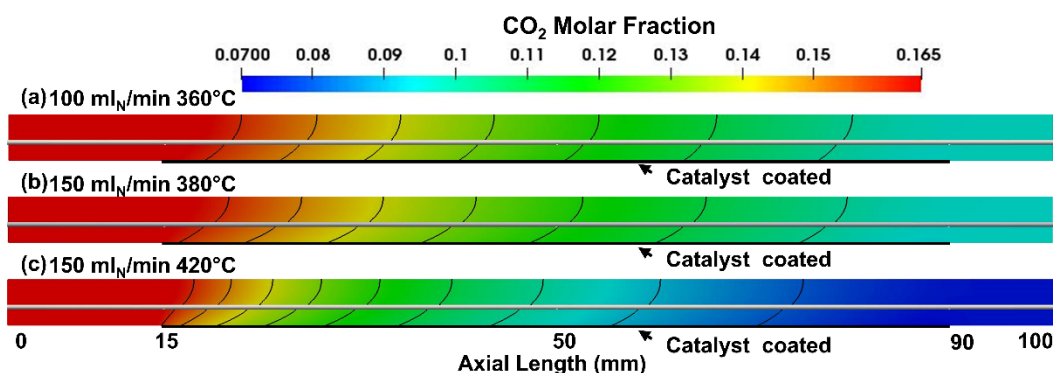


Fig. 3 CO₂ mole fraction contours for the catalytic plate reactor on a vertical slice along the center of the CPR operating at 1.2 bar_{abs}, suction of 2 ml/min and (a) 100 ml_N/min at 360 °C, (b) 150 ml_N/min at 380 °C, (c) 150 ml_N/min at 420 °C.

3.2 Effect of flow distributor channels and flow rate

The three flow distribution channels upstream of the CPR's rectangular reactor zone influence the flow development. This effect dictates the final spatial range of the measured concentration data that can be used for kinetic studies. The submerged jets generated by the fluid leaving the distributor channels create recirculations in the inlet region for the 300 ml_N/min flow rate case, visualized by the blue-coloured axial velocity profile (negative values) in Fig. 4a. With a lower flow rate (i.e., 100 ml_N/min), the jet region is considerably smaller with little to no recirculation (Fig. 4b). This reduction in the recirculation zone is also observed for the lower flow rate (i.e., 100 ml_N/min) case operated at 4 bar_{abs} (Fig. 4c). The inlet effects zone is associated with the local

recirculation of flow at the reactor's entrance region. The influence of submerged jets on the axial velocities is observed in the initial 10 mm of the domain is due to the increase in cross-sectional area as the flow enters the reactor domain from the inlet distribution channels. The side-facing orientation of the two main inlets and flow obstruction in the central distribution channel due to the presence of sampling capillary drives 75% of the total volumetric flow through the outer two distributor channels (Fig. 4).

A uniform flow field is necessary to facilitate the analysis of the kinetic data by means of simple reactor models. Therefore, avoiding flow non-idealities close to the catalytic surface is important to achieve a uniform residence time in the reactor. In this view, we have analyzed the fluid flow close to the inlet channels aiming at defining the region of the CPR where fully developed conditions are reached. The developed flow zone corresponds to the region with stable axial velocities and is most suitable for extracting the local composition data, and this zone exists between the inlet and outlet zones.

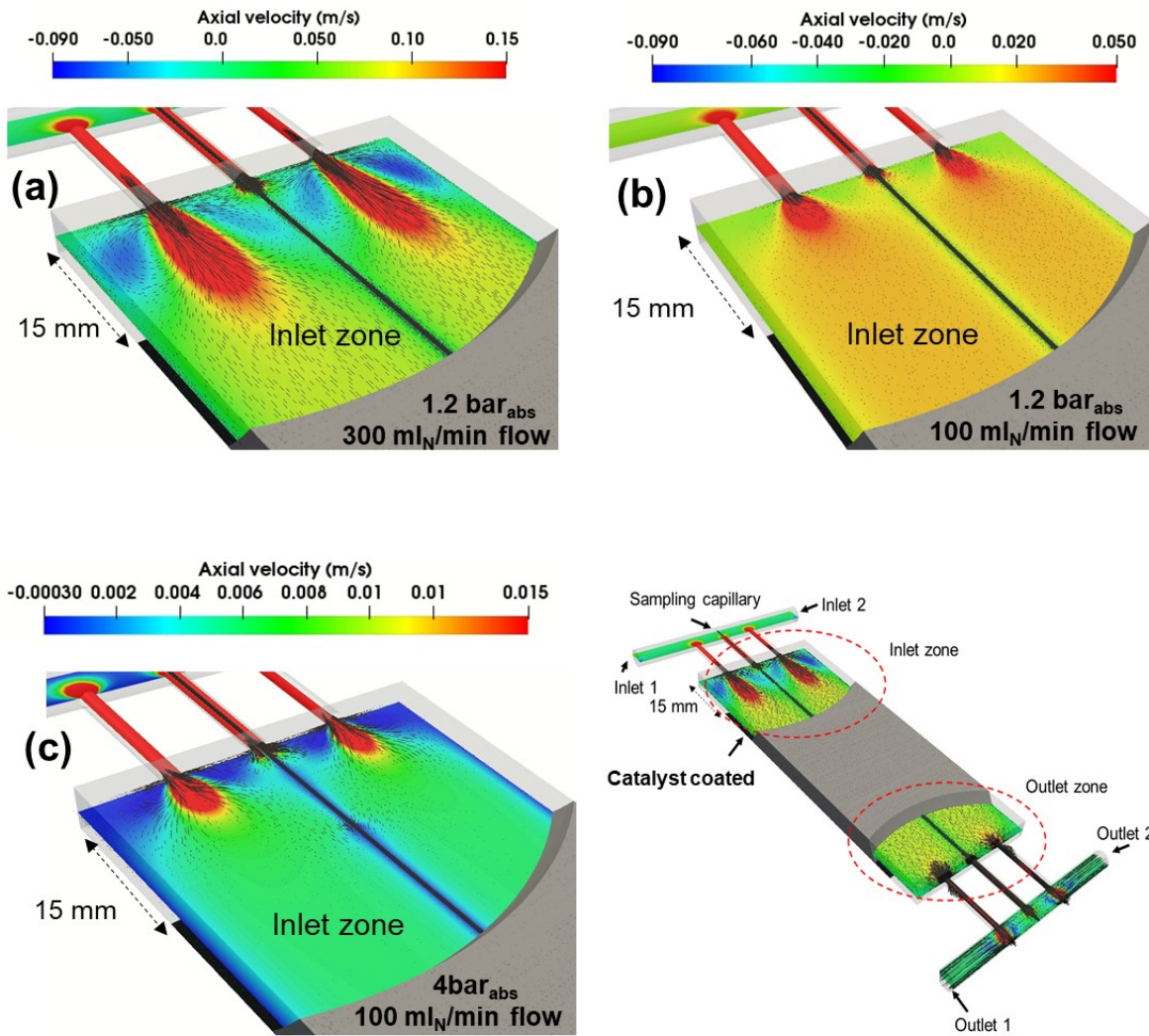


Fig. 4 Velocity contours/vectors along horizontal planes passing through the center of the CPR operating at 360° C and 1.2 bar_{abs}, with 2 ml/min suction. Zoom in at the inlet domain for a total flow rate of (a) 300 ml_N/min with and 1.2 bar_{abs}, (b) 100 ml_N/min and 1.2 bar_{abs}, and (c) 100 ml_N/min and 4 bar_{abs}.

The flow development in this zone is shown in Fig. 5 and Fig. 6 for the axial velocities along the channel height (y -direction) and channel width (x -direction), respectively. In Fig. 5, the axial location “0” denotes the beginning of the reactor domain (downstream of distributor channels). The slice location x_1 is along the center of the outer distributor channel, which has no sampling capillary, and location x_2 at an x -location that is in between the outer and central distributor channel. Flow fully develops and forms a parabolic velocity profile by 20 mm into the reactor

domain for both these locations. Lower velocity is observed at $z = 5$ mm on location x2 as this line is not directly facing a distributor channel flow. This local effect gets stabilized within the initial 30% of the reactor's length for the upper extreme of 300 ml_N/min. Similar effects are observed in the outlet effects zone due to the convergence of the flow into the three collector channels.

Fig. 6 shows axial velocity on horizontal lines located at a length of 5, 10, 20, 30 and 40 mm into the rectangular CPR domain. This plot serves as a good estimate of the flow development over the catalytic surface, and it is evident that the flow fully gets stabilized by 20 mm into the CPR domain. Fig. 6 can be analyzed along with the Fig. 5 to identify the axial location at which the flow can be considered as fully developed along both the horizontal and the vertical planes in the reactor. Based on this analysis, the region between 30 mm and 85 mm from the total available 100 mm length of the rectangular region is independent of local flow phenomena (i.e., max flow rate of 300 ml_N/min) and can be safely used for extracting kinetic data (i.e., gas composition). Fig. S4 shows the axial velocity in the z -direction in the CPR domain for cases with and without any suction.

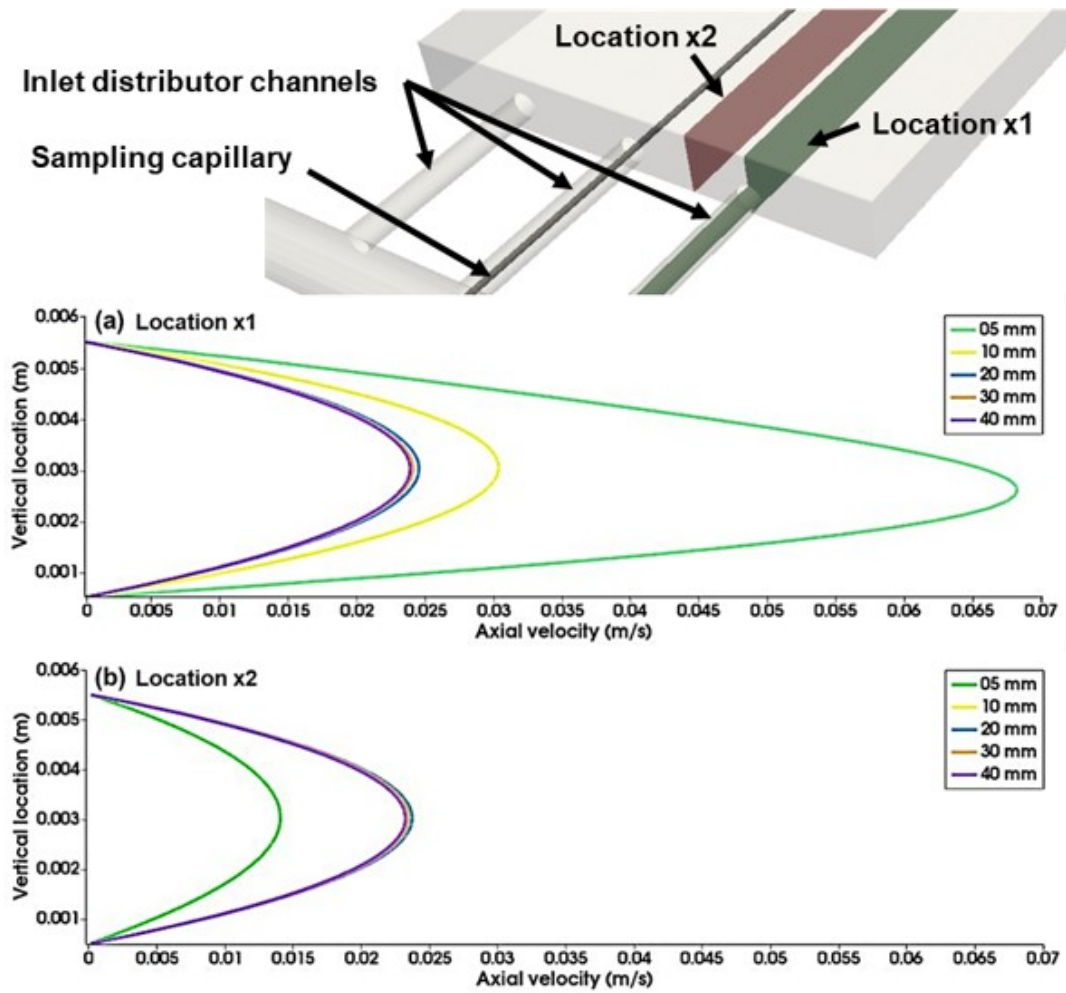


Fig. 5 Axial velocity at different vertical lines (located at $z = 5, 10, 20, 30$ and 40 mm) on an axial slice (a) Location x1; passing through mid of the outer distributor channel, (b) Location x2; passing through the location in between outer and central distributor channel, operating at $100 \text{ ml}_N/\text{min}$, $360 \text{ }^\circ\text{C}$ and $1.2 \text{ bar}_{\text{abs}}$, with $2 \text{ ml}/\text{min}$ suction.

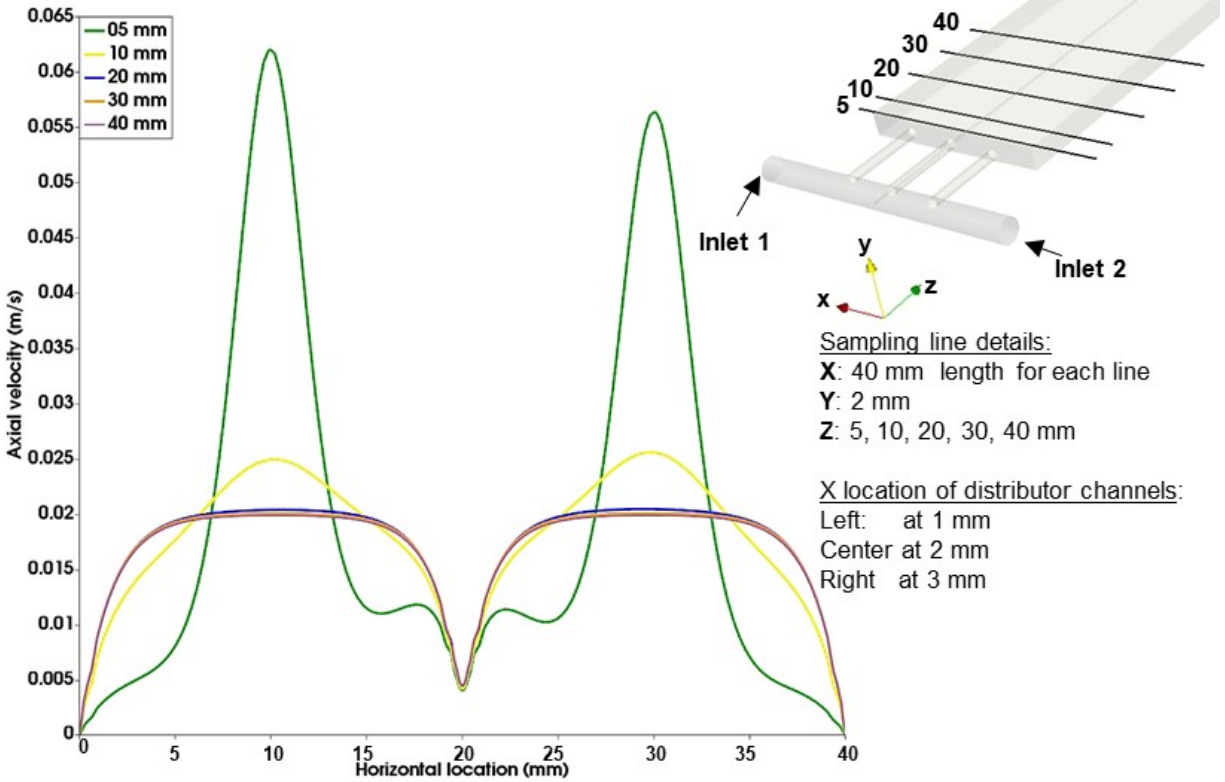


Fig. 6 Axial velocity at different vertical lines (located at $z = 5, 10, 20, 30$ and 40 mm) on a horizontal slice at an elevation of 2 mm above the coated surface, operating at $100 \text{ ml}_N/\text{min}$, $360 \text{ }^\circ\text{C}$ and $1.2 \text{ bar}_{\text{abs}}$, with $2 \text{ ml}/\text{min}$ suction.

3.3 Effect of suction

The suction created by the mass spectrometer through the capillary might affect the quality of the collected data. The suction zone is a region that is directly below the sampling port, and it is influenced by suction of the downward-facing sampling capillary. Fig. 7 illustrates the streamline made by the capillary suction 1 mm above the catalyst surface with an area of 10×6.5 mm. The orifice of the capillary is located at the axial position of 15 mm.

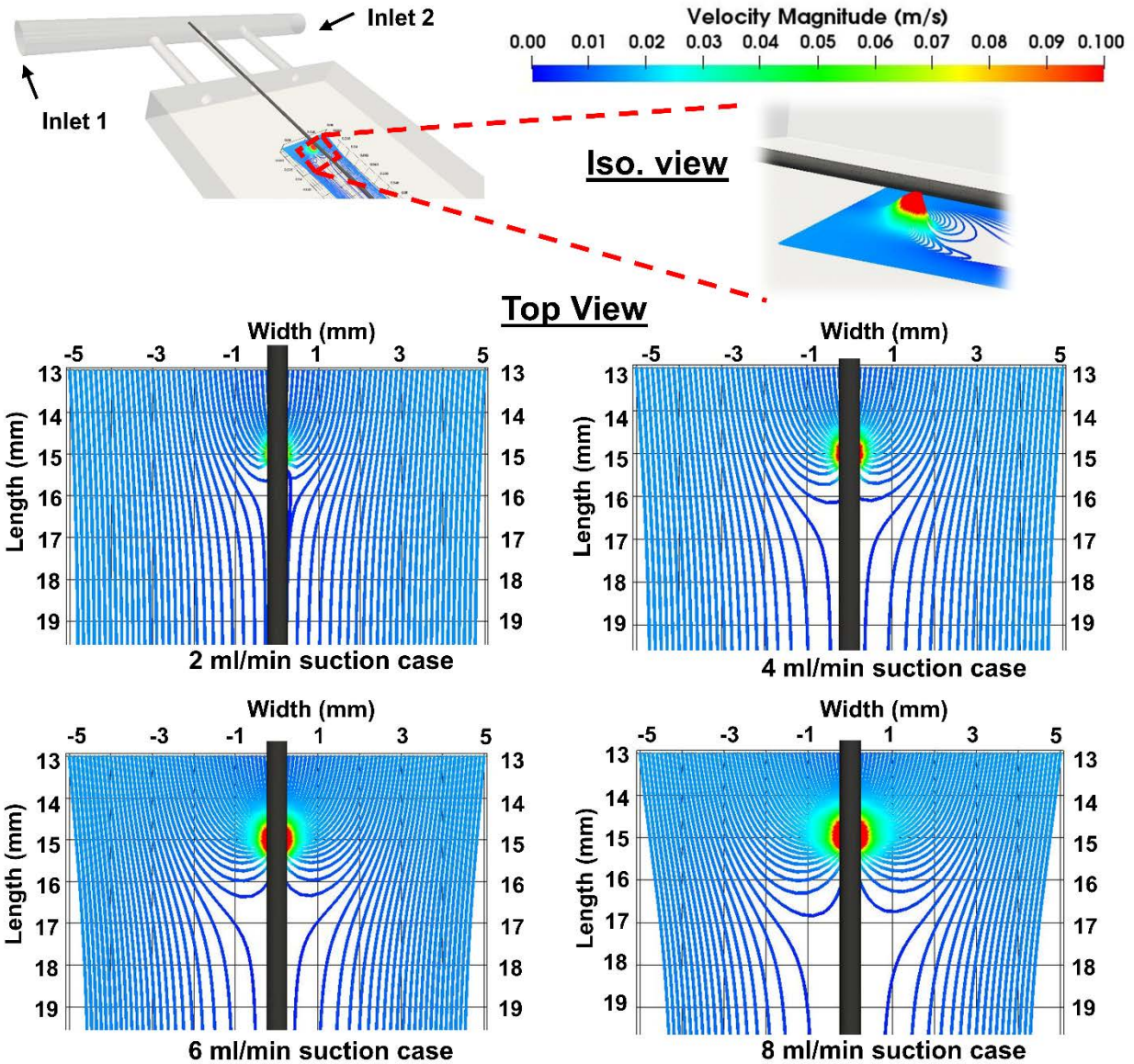


Fig. 7 Velocity streamlines from a horizontal line source in the catalytic plate reactor (CPR) operating at 360 °C, 1.2 bar_{abs}, 100 ml_N/min, and suction varying between 2 to 8 ml/min.

A cone-shaped suction zone with the upward flow (positive y-direction velocities) is created below the orifice port for all the investigated suction flow rates of 2 ml/min to 8 ml/min with bulk flow rates ranging between 100 and 300 ml_N/min. This conical zone is characterized as a region with a minimum upward velocity ratio of ~5 times with respect to the bulk flow in z-direction, and it serves as a reasonable qualitative estimate of the zone of influence of suction. The base area of this conical zone is found to increase with the increase in the suction flow rate through the port,

and it increases from less than a diameter of ± 1 mm for the 2 ml/min suction case to slightly larger than a diameter of ± 1 mm for the 4 ml/min and to a maximum of about a diameter of ± 2 mm for the 8 ml/min suction case (Fig. 8). Moreover, a positive velocity peak is observed before the orifice location due to the accelerated flow towards the orifice, while the negative value observed upstream of the sampling port is caused by backflow due to the suction.

A quantitative assessment of suction on the sampling species concentration is provided in Fig. 8. It reports the contours of mass flux in the y -direction (direction of the suction orifice) at different elevations overlaid on the velocity vector at these locations. The suction of the sampling capillary operates between 1 to 2 ml/min at atmospheric pressure, and the 8 ml/min suction case represents an upper extreme. The mass flux increased by a factor of 100 from the base plane near the catalyst surface ($Y = 1$) to the elevation of $Y = 2$ mm in all the range of suction flowrates (i.e., 2 to 8 ml/min). For the 8 ml/min case, the velocity vectors were symmetric, indicating a suction of material between 1 mm upstream and 1 mm downstream of the suction orifice. 2 ml/min suction case did not exhibit this symmetry as the driving force created by the suction was not sufficient to overcome the axial bulk flow (z -direction) in the domain. In all the suction scenarios, the product species in the vicinity of the sampling port were extracted by the suction, and their presence near the port was primarily governed by the mass transfer from the catalytic surface. Analogous to the inverse Peclet number, the ratio of diffusive flux to convective flux (capillary suction) in the upward y -direction was evaluated between the catalyst layer and the sampling capillary to quantify whether diffusion or convection is dominant. The ratio of diffusive flux to convective flux was found to be between 100 to 10,000. Hence, it is evident that during the operation of the suction port, the mass species diffusion is not limiting. This is also in agreement with the evaluation that

the mass transfer (y-direction) was much fast than the surface reaction (i.e., experiments were conducted in the kinetic regime) [13].

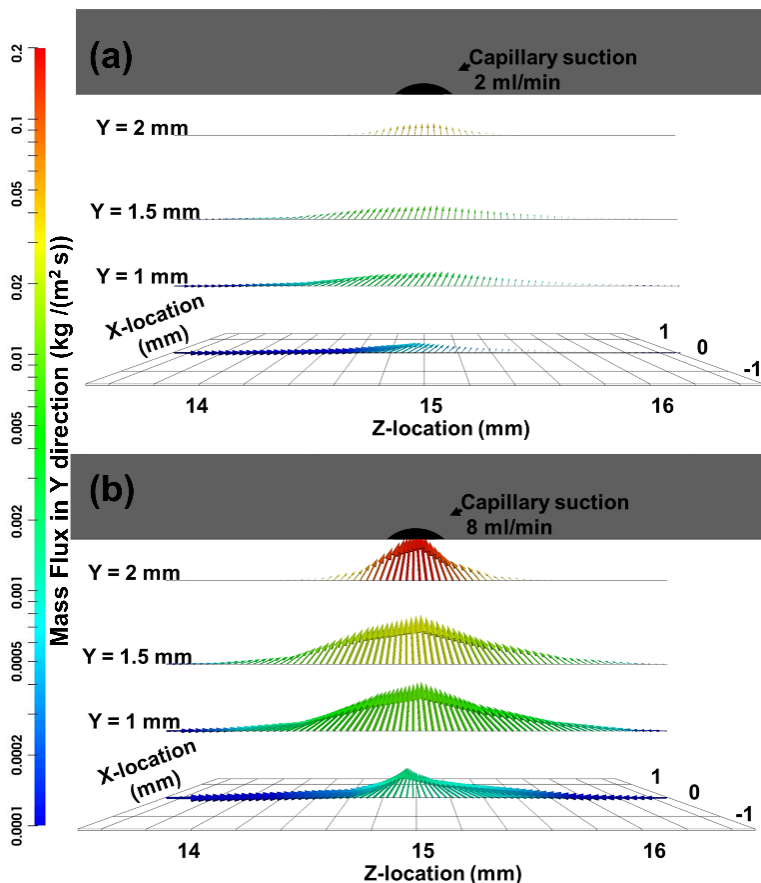


Fig. 8 Velocity vectors along three horizontal lines ($y = 1.0, 1.5,$ and 2.0 mm) colored by the mass flux in y -direction for the catalytic plate reactor (CPR) operating at $360\text{ }^{\circ}\text{C}$, $1.2\text{ bar}_{\text{abs}}$ and $100\text{ ml}_N/\text{min}$. (a) $2\text{ ml}/\text{min}$ suction and (b) $8\text{ ml}/\text{min}$ suction.

The effect of sampling location is investigated by moving the capillary orifice to three locations along the reactor axis, namely Z1 (beginning of catalyst coated length), Z2 (midway along the catalyst coated length), and Z3 (end of catalyst coated length). $2\text{ ml}/\text{min}$ suction case shows identical mass flux at three elevations ($y = 1.0\text{ mm}, 1.5\text{ mm},$ and 2.0 mm) for Z1, Z2, and Z3 orifice locations (Fig.S5 of the supplementary material). It agrees with the observation that the bulk flow gets fully developed by the time it reaches point Z1 and continues to be stable till Z3. The capillary

orifice axial location has no effect on the region's sampling capability in the fully developed flow region.

The effect of the suction on the composition profile is further investigated, as shown in Fig. 9, by comparing the CO₂ mole fraction predictions along the reactor axis on the sample zone line and the reference zone line. This figure also includes the experimental CO₂ values along the sample zone line. The sample zone line is an axial line (z -direction) located 0.1 mm below the sampling capillary, and the reference zone line is created by translating the sampling zone line by 10 mm in positive x -direction while keeping the vertical distance (y -direction) constant. The CO₂ molar fractions are identical at both of these locations and continue to match along the entire length of the reactor. This similarity is attributed to the high rate of species transfer and is also valid for the higher bulk flow rate of 300 ml_N/min. This proves that the sampling capillary does indeed gather correct kinetic data.

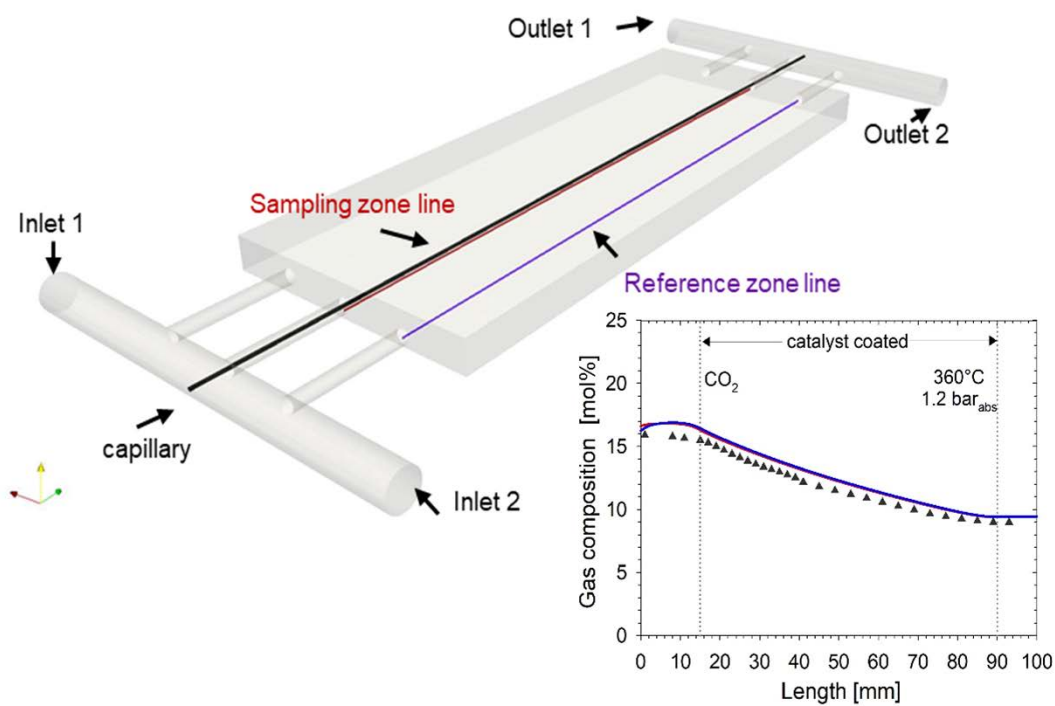


Fig. 9 CO₂ species molar fraction along the length of the CPR for sampling and reference zone. Symbols denote experimental data while solid lines the CFD model. Operating condition: 360 °C, 1.2 bar_{abs}, 100 ml_N/min, and suction of 2 ml/min.

Fig. 10 shows the CO₂ molar fraction for the CPR reactor operating at 360 °C, 1.2 bar_{abs}, 100 ml_N/min. Fig.S6 shows the CH₄ molar fraction profile for the same case. The consumption of CO₂ on the catalytic plate leads to curved iso-contours in the vertical direction. This curved nature is observed along all the axial slices of the CPR domain, including the reference zone and the central sampling zones. A slightly higher slope is observed along the central sampling zone due to the reduced bulk flow rate from the capillary tube's presence, although the overall difference between the species molar fraction at same elevation in these two zones is always < 1% points. This variation in species profile between central and side regions is marginally changed with cases with higher bulk flow rates. For 100 ml_N/min bulk flow, species concentration varied by approximately 0.2 % points from the catalyst plate to the capillary orifice, and for 300 ml_N/min bulk flow, this

concentration variation increased by 0.25% points. Hence, the quality of the gathered kinetic data is not significantly affected at higher bulk flow rates when sampling is done. As a whole, the concentration values obtained in the suction measurement are an average of concentration in the vertical y -direction driven by the high upward species diffusion flux. This observation concurs with the 2D process model predictions made by Hernandez Lalinde *et al.* [13] for the same chemistry in the CPR. This small change in concentration along the width and height at a specific axial position of the CPR makes sampling capillary with downward/sideward/upward orientation of sampling port identical in performance.

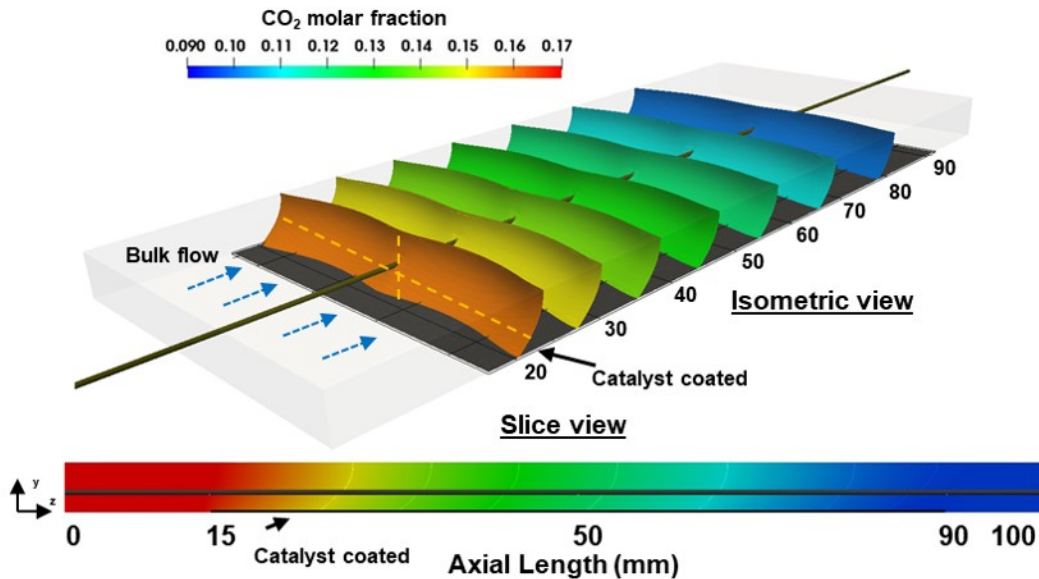


Fig. 10 CO₂ molar fraction contours for the catalytic plate reactor (CPR) operating at 360 °C, 1.2 bar_{abs}, 100 ml_N/min, and suction of 2 ml/min.

3.4 Effect of an open-ended capillary for sampling

The flow field in the CPR inlet region with the open-ended capillary varies from the CPR with conventional continuous end-to-end capillary. This difference is primarily due to the absence of the capillary upstream of the sampling point and it causes the bulk flow to split equally among the

three distribution channels (Fig. S1). This phenomenon does not occur in the CPR with end-to-end capillary as a portion of the capillary obstructs the flow in the central distributor channel.

Fig. 11 shows the velocity vectors along certain horizontal lines below the capillary and on two vertical lines upstream of the capillary suction orifice for the 100 mL_N/min bulk flow case. The suction at the tip of the open-ended capillary has a minimal impact (i.e., negligible y-velocities), and it is evident from the minimal upward velocity vectors at $y = 1.0, 1.5,$ and 2.0 mm locations. The flow in the CPR domain is fully developed at an axial location that is 1.2 mm upstream of the suction orifice (Z1). This is confirmed by the parabolic velocity profile at this location with a peak axial velocity of 0.035 m/s. Whereas at 0.7 mm upstream of the orifice (Z2), the velocity profile near the port is slightly distorted. In the open-ended case, the effect of suction is limited to 0.5 mm upstream of the orifice and is 50% more localized with respect to length from the sampling location in comparison to an identical flow case with CPR reactor having an end-to-end capillary. In the open-ended mode of operation, the bulk flow and the sampling orifice suction are aligned in the same direction, and this keeps the zone of influence of the suction small even at higher suction rates. Based on the results shown in Section 3.3 above, the impact of suction is highly localized and yields an average value of species concentration of species for the range of 100-300 mL_N/min bulk flow and suction of 2-8 mL/min. In the scope of the experiments that are conducted on CPR, both open ended and continuous sampling approaches performed similarly. In detail, the concentration predictions at a specific axial location for both approaches of capillary operation agreed with each other with $< 5\%$ variation. This is in agreement with our observations in the CPR with an end-to-end capillary, as the concentration profiles of CO₂ agree reasonably well along the reference zone line and the sampling zone (see Fig. 9), despite the slight difference in the flow rate in these two regions. Both these observations indicate the existence of a chemical regime in

the current operating conditions. The continuous capillary approach overcomes the capillary bending issue of the open-ended capillary design caused due to the unsupported front end.

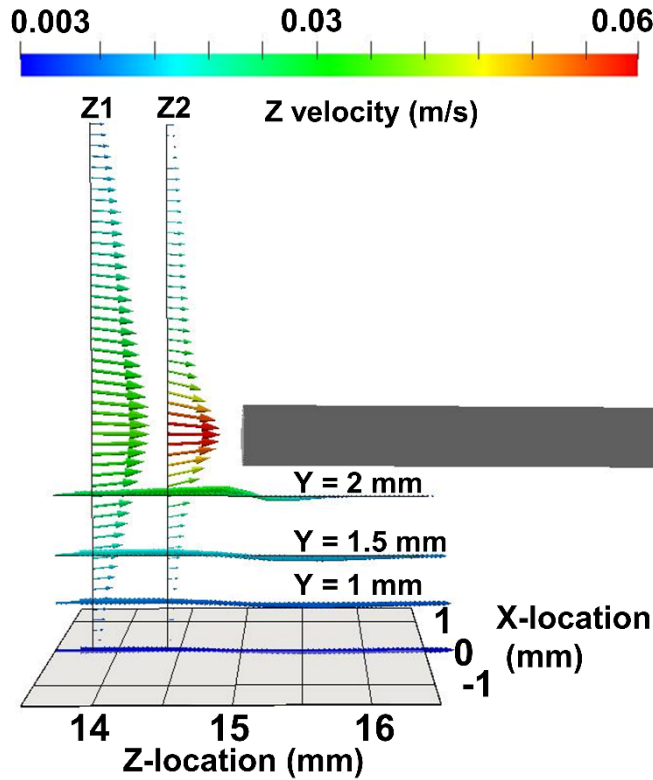


Fig. 11 Velocity vectors on 3 horizontal lines ($Y = 1.0, 1.5,$ and 2.0 mm) and two vertical lines for the catalytic plate reactor (CPR) operating at $360\text{ }^{\circ}\text{C}$, $1.2\text{ bar}_{\text{abs}}$, $100\text{ ml}_N/\text{min}$, and suction of $2\text{ ml}/\text{min}$.

3.5 Effect of dummy capillaries

The presence of the sampling capillary creates a flow maldistribution in the inlet distributor channels that results in 75% of the total bulk flow going through the two outer channels, and a maximum axial velocity of 0.82 m/s is observed in the outer distributor channels and 0.26 m/s in the central distributor channels for a total flow rate of $100\text{ ml}_N/\text{min}$ at $360\text{ }^{\circ}\text{C}$ and $1.2\text{ bar}_{\text{abs}}$ (see Fig. 12b). This maldistribution can be corrected by enforcing an equal cross-sectional area in each of these channels by means of dummy capillaries on the left and right-hand sides with the same diameter as the sampling capillary. These dummy capillaries are shorter than the sampling

capillary and terminate at the beginning of the reactor domain (see Fig. 12a). The CFD modeling result shows that the flow is equally distributed (~33%) with the introduction of the dummy capillaries, and the jets created at the end of each inlet distributor channel are very similar (Fig. 12c). Within all three distributor channels the maximum axial velocity is the same with a value of 0.55 m/s for the same inlet flow rate of 100 ml_N/min at 360 °C. The velocity contours have been clipped at a maximum axial velocity of 0.05 m/s to show the submerged jets and the negative velocity region. By introducing the dummy capillaries the recirculation zones with negative axial velocities in the inlet region are significantly reduced, which allows to use of CPR for kinetic experiments at higher bulk flow rates (> 300 ml_N/min). The elevation (y-location) selected for this slice passes through the middle of the central sampling capillary. The cases shown in Fig. 12 yielded identical gas composition profiles along the length of the reactor (not shown). This agrees with the observation in Fig. 9 for the single continuous capillary case, where almost identical species profiles exist along the central and reference zone lines despite the difference in the bulk flow. Based on these results, modifying the CPR design with two dummy capillaries could only slightly improve its operational range for kinetic studies.

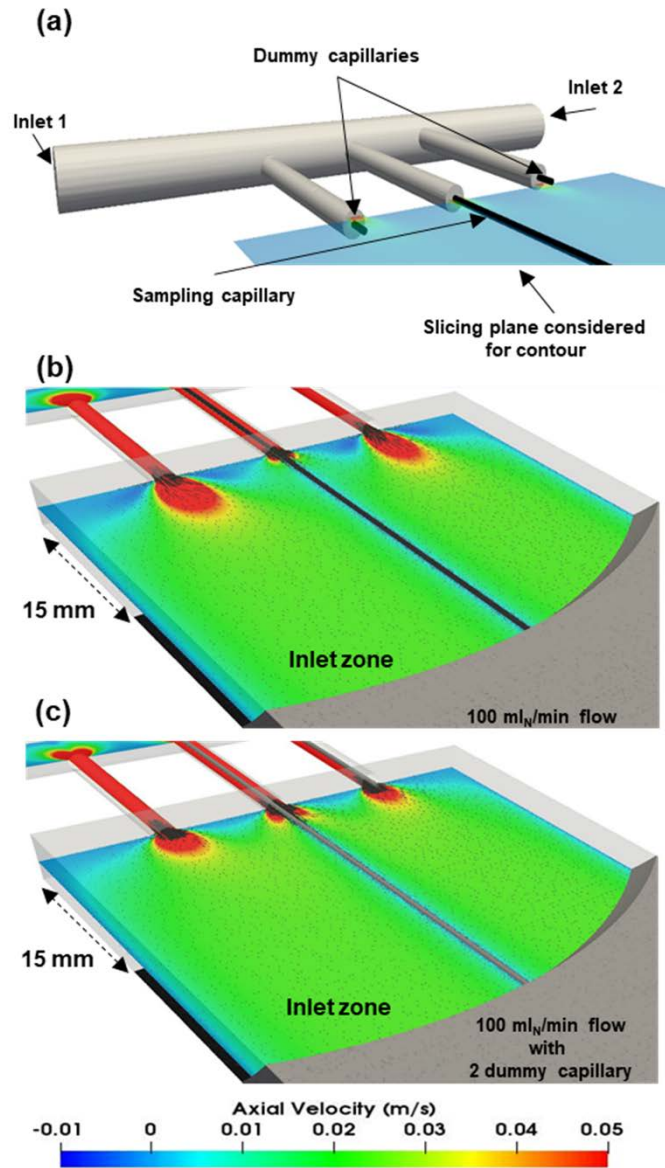


Fig. 12 (a) Position of the two dummy capillaries that are present above and below the sliced plane for plotting velocity contour. Velocity contours along horizontal planes for the case (b) without and (c) with dummy capillaries in the outer two distributor channels. Operating conditions are 100 ml_N/min, 360 °C, 1.2 bar_{abs} and 2 ml/min suction.

4 Conclusions

The present CFD study confirms that the presence of the movable sampling capillary (suction probe) within the rectangular channel domain of the CPR has a negligible effect on the flow and gas species distribution and, as such, does not falsify the kinetic data. The axial gas composition profile is essentially the same compared to a profile along an equivalent reference zone without a capillary. The bulk flow in the range of 100-300 ml_N/min is optimal for conducting kinetic experiments as the flow develops relatively quickly. The species diffusion and recirculation in the entrance region (within the first 15 mm) of the rectangular domain is shown to matter, but the rest of the channel (85-95% of the length) can safely be used for kinetic data acquisition without the need for any correction function that are required for monolithic systems. The suction itself does not impact the bulk flow significantly within the operating range of 1-8 ml/min suction. Moreover, the continuous capillary with a side orifice and the open-ended capillary configuration yield the same results. Lastly, it is proven that the measured gas concentration reflects the average gas concentrations along the channel height, which enables the use of a one-dimensional model for the kinetic parameter estimation. In summary, the presented catalytic plate reactor with spatially resolved measurement techniques is very suitable for the kinetic study of heterogeneously catalyzed reactions.

Notation

A	[m ²]	geometric area
A_{cat}^{eff}	[m ²]	effective catalytic area
g	[m/s]	acceleration vector due to gravity

ΔH_R^0	[kJ/mol]	standard heat of reaction
NCG	[-]	number of gas-phase species
p	[bar]	pressure
r_{CO_2meth}	[mol/(kg _{cat} s)]	rate of reaction (CO ₂ methanation)
r_{RWGS}	[mol/(kg _{cat} s)]	rate of reaction (reversed water gas shift)
t	[min]	time
T	[°C]	temperature
V_k	[-]	diffusion velocity
I	[-]	identity tensor
ρ	[kg/m ³]	density
μ	[kg/(m s)]	dynamic viscosity
v	[m/s]	velocity vector
ω_k	[-]	mass fraction of gas-phase species k
$\dot{\Omega}_k^{het}$	[mol/s]	formation rate due to the surface reactions
$\Gamma_{k,mix}$	[m ² /s]	individual species mixture averaged diffusion coefficient

Associate content

End-to-end and open-ended capillary CPR configurations (Fig.S1). Slice view of meshes used for mesh-independency study (Fig.S2). Observed and mesh depended calculated axial CO₂ gas composition profiles (Fig.S3). Axial gas velocity profile within the CPR as function of total flow

rate (Fig.S4). Sampling port locations (Fig.S5). 3D CH₄ gas concentration profile at 360 °C and 1.2 bar_{abs}, (Fig.S6).

Declaration of Competing Interest

The authors declare that they have no known competing financial interests or personal relationships that could have influenced the work reported in this paper.

Acknowledgments

The authors thank financial support from the Natural Sciences and Engineering Research Council (NSERD) and Mitacs Globalink Award for this study. Compute Canada and CINECA clusters for the computational resources.

References

- [1] J.-S. Choi, W.P. Partridge, C.S. Daw, Spatially resolved in situ measurements of transient species breakthrough during cyclic, low-temperature regeneration of a monolithic Pt/K/Al₂O₃ NO_x storage-reduction catalyst, *Appl. Catal., A*. 293 (2005) 24–40.
<https://doi.org/10.1016/j.apcata.2005.06.025>.
- [2] J.-S. Choi, W.P. Partridge, W.S. Epling, N.W. Currier, T.M. Yonushonis, Intra-channel evolution of carbon monoxide and its implication on the regeneration of a monolithic Pt/K/Al₂O₃ NO_x storage-reduction catalyst, *Catalysis Today*. 114 (2006) 102–111.
<https://doi.org/10.1016/j.cattod.2006.02.011>.
- [3] D. DalleNogare, N.J. Degenstein, R. Horn, P. Canu, L.D. Schmidt, Modeling spatially resolved profiles of methane partial oxidation on a Rh foam catalyst with detailed

- chemistry, *Journal of Catalysis*. 258 (2008) 131–142.
<https://doi.org/10.1016/j.jcat.2008.06.006>.
- [4] R. Horn, N.J. Degenstein, K.A. Williams, L.D. Schmidt, Spatial and temporal profiles in millisecond partial oxidation processes, *Catalysis Letters*. 110 (2006) 169–178.
<https://doi.org/10.1007/s10562-006-0117-8>.
- [5] J. Touitou, K. Morgan, R. Burch, C. Hardacre, A. Goguet, An in situ spatially resolved method to probe gas phase reactions through a fixed bed catalyst, *Catalysis Science & Technology*. 2 (2012) 1811. <https://doi.org/10.1039/c2cy20141k>.
- [6] J. Touitou, R. Burch, C. Hardacre, C. McManus, K. Morgan, J. Sá, A. Goguet, An in situ spatially resolved analytical technique to simultaneously probe gas phase reactions and temperature within the packed bed of a plug flow reactor., *The Analyst*. 138 (2013) 2858–62. <https://doi.org/10.1039/c3an00250k>.
- [7] J. Kopyscinski, T.J. Schildhauer, S.M.A. Biollaz, Fluidized-Bed Methanation: Interaction between Kinetics and Mass Transfer, *Industrial & Engineering Chemistry Research*. 50 (2011) 2781–2790. <https://doi.org/10.1021/ie100629k>.
- [8] J. Kopyscinski, T.J. Schildhauer, S.M.A. Biollaz, Methanation in a fluidized bed reactor with high initial CO partial pressure: Part I—Experimental investigation of hydrodynamics, mass transfer effects, and carbon deposition, *Chem. Eng. Sci.* 66 (2011) 924–934. <https://doi.org/10.1016/j.ces.2010.11.042>.
- [9] A. Maghsoumi, A. Ravanelli, F. Consonni, F. Nanni, A. Lucotti, M. Tommasini, A. Donazzi, M. Maestri, Design and testing of an operando-Raman annular reactor for kinetic

- studies in heterogeneous catalysis, *Reaction Chemistry & Engineering*. 2 (2017) 908–918.
<https://doi.org/10.1039/C7RE00092H>.
- [10] M. Bosco, F. Vogel, Optically accessible channel reactor for the kinetic investigation of hydrocarbon reforming reactions, *Catalysis Today*. 116 (2006) 348–353.
<https://doi.org/10.1016/j.cattod.2006.05.064>.
- [11] J. Kopyscinski, T.J. Schildhauer, F. Vogel, S.M.A. Biollaz, A. Wokaun, Applying spatially resolved concentration and temperature measurements in a catalytic plate reactor for the kinetic study of CO methanation, *Journal of Catalysis*. 271 (2010) 262–279.
<https://doi.org/10.1016/j.jcat.2010.02.008>.
- [12] J. Hernandez Lalinde, K. Kofler, X. Huang, J. Kopyscinski, Improved Kinetic Data Acquisition Using An Optically Accessible Catalytic Plate Reactor with Spatially-Resolved Measurement Techniques. Case of Study: CO₂ Methanation, *Catalysts*. 8 (2018) 86. <https://doi.org/10.3390/catal8020086>.
- [13] J.A. Hernandez Lalinde, P. Roongruangsree, J. Ilsemann, M. Bäumer, J. Kopyscinski, CO₂ methanation and reverse water gas shift reaction. Kinetic study based on in situ spatially-resolved measurements, *Chemical Engineering Journal*. 390 (2020) 124629.
<https://doi.org/10.1016/j.cej.2020.124629>.
- [14] M. Hettel, C. Diehm, B. Torkashvand, O. Deutschmann, Critical evaluation of in situ probe techniques for catalytic honeycomb monoliths, *Catal. Today*. 216 (2013) 2–10.
<https://doi.org/10.1016/j.cattod.2013.05.005>.
- [15] J. Sa, D.L.A. Fernandes, F. Aiouache, A. Goguet, C. Hardacre, D. Lundie, W. Naeem, W.P. Partridge, C. Stere, SpaciMS: spatial and temporal operando resolution of reactions

- within catalytic monoliths, *Analyst*. 135 (2010) 2260–2272.
<https://doi.org/10.1039/C0AN00303D>.
- [16] W. Benzinger, E. Daymo, M. Hettel, L. Maier, C. Antinori, P. Pfeifer, O. Deutschmann, Reverse water gas shift (RWGS) over Ni – Spatially-resolved measurements and simulations, *Chemical Engineering Journal*. 362 (2019) 430–441.
<https://doi.org/10.1016/j.cej.2019.01.038>.
- [17] M. Maestri, A. Cuoci, Coupling CFD with detailed microkinetic modeling in heterogeneous catalysis, *Chemical Engineering Science*. 96 (2013) 106–117.
<https://doi.org/10.1016/j.ces.2013.03.048>.
- [18] H.G. Weller, G. Tabor, A tensorial approach to computational continuum mechanics using object-oriented techniques, 12 (1998).
- [19] A. Aljishi, G. Veilleux, J.A.H. Lalinde, J. Kopyscinski, The effect of synthesis parameters on ordered mesoporous nickel alumina catalyst for CO₂ methanation, *Applied Catalysis A: General*. 549 (2018) 263–272. <https://doi.org/10.1016/j.apcata.2017.10.012>.
- [20] J.A. Hernandez Lalinde, J. Jiang, G. Jai, J. Kopyscinski, Preparation and characterization of Ni/Al₂O₃ catalyst coatings on FeCrAl-loy plates used in a catalytic channel reactor with in-situ spatial profiling to study CO₂ methanation, *Chemical Engineering Journal*. 357 (2019) 435–446. <https://doi.org/10.1016/j.cej.2018.09.161>.
- [21] M.R.J. Charest, C.P.T. Groth, Ö.L. Gülder, A computational framework for predicting laminar reactive flows with soot formation, *Combustion Theory and Modelling*. 14 (2010) 793–825. <https://doi.org/10.1080/13647830.2010.512960>.

- [22] C.F. Curtiss, J.O. Hirschfelder, Transport Properties of Multicomponent Gas Mixtures, *JChPh.* 17 (1949) 550–555. <https://doi.org/10.1063/1.1747319>.
- [23] Molecular theory of gases and liquids. J. O. Hirschfelder, C. F. Curtiss, and R. B. Bird. Wiley, New York, 1954. 1219 pp, *JPoSc.* 17 (1955) 116–116. <https://doi.org/10.1002/POL.1955.120178311>.
- [24] R.J. Kee, F.M. Rupley, E. Meeks, J.A. Miller, CHEMKIN-III: A FORTRAN chemical kinetics package for the analysis of gas-phase chemical and plasma kinetics, (1996). <https://doi.org/10.2172/481621>.
- [25] M. Bracconi, M. Ambrosetti, M. Maestri, G. Groppi, E. Tronconi, A fundamental investigation of gas/solid mass transfer in open-cell foams using a combined experimental and CFD approach, *Chemical Engineering Journal.* 352 (2018) 558–571. <https://doi.org/10.1016/J.CEJ.2018.07.023>.
- [26] D. Micale, C. Ferroni, R. Uglietti, M. Bracconi, M. Maestri, Computational Fluid Dynamics of Reacting Flows at Surfaces: Methodologies and Applications, *Chemie Ingenieur Technik.* (2022). <https://doi.org/10.1002/CITE.202100196>.
- [27] A. Ribes, C. Caremoli, Salome platform component model for numerical simulation, *Undefined.* 2 (2007) 553–564. <https://doi.org/10.1109/COMPSAC.2007.185>.